Finally we obtain the enstrophy flux through the nth octave in Fourier space:

$$\Pi_n^{(\Omega)} = \frac{\Omega_n}{\tau_n} \sim \frac{\mathrm{k}_n^3 E(k_n)}{\left(\mathrm{k}_n^3 E(k_n)\right)^{-1/2}} \qquad (2.82)$$

If we assume that this is constant in a steady state and independent of n, then $\eta \sim \Pi_n^{(\Omega)}$ and we obtain the spectrum in the constant enstrophy flux regime:

$$E(k) \sim \eta^{2/3} k^{-3} \qquad (2.83)$$

Using either dimensional analysis or the Tauberian theorems (Box 2.2), we can obtain the corresponding real-space result:

$$\Delta v \approx \eta^{1/3} \Delta x \qquad (2.84)$$

These formulae (sometimes called the "Kraichnan" laws; Kraichnan, 1967) need some refinement since the picture of enstrophy being passed mainly from one octave to a neighbouring octave (without sign-ificant direct, nonlocal transfer over many octaves) is only strictly valid if the cascade was local, $\beta < 3$. Since we have found $\beta = 3$, we may anticipate that this "marginal" case will involve at least logarithmic corrections. This is indeed the case.`

The result $\beta = 3$ shows that every octave in two dimensional turbulence contributes approximately equally (to within the log corrections) to the non-linear dynamics, the cascade is on the borderline between local and nonlocal. Each eddy turnover time τ_n is approximately equal. Note that the non-localness of two-dimensional cascades is quite serious; for example (Kevlahan and Farge, 1997), numerical simulations on 1024×1024 grids with the usual Newtonian viscosity dissipation term (i.e. a Laplacian) find $\beta \approx 4$ or larger depending on the boundary conditions, but $\beta \approx 3$ for various higher powers (up to 8th) of a Laplacian (i.e. using "hyperviscosity"). This implies that the spectral exponent β depends on the details of the dissipation term. Due to the effects of nonlocalness, two-dimensional turbulence is thus in many ways more complex than three-dimensional turbulence, and since no clear direct evidence for a two-dimensional cascade has been found in the atmosphere (or in other geophysical
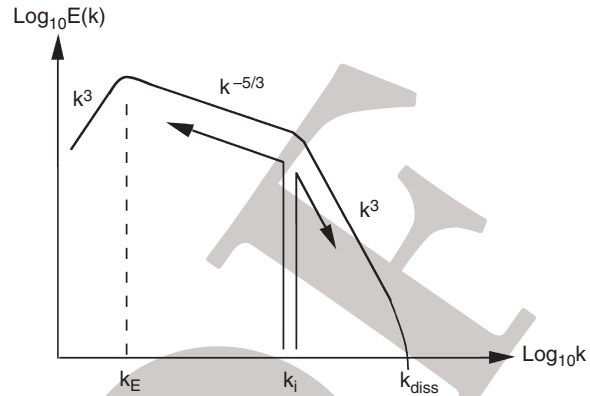

Fig. 2.8 A schematic illustration of the 2D enstrophy cascade with both energy and enstrophy fluxes injected at wavenumber k_i. The energy flux is cascaded to lower wavenumbers while the enstrophy flux is cascaded to higher wavenumbers.

systems), its status as a useful geophysical model is uncertain (it may, however, be relevant in soap films: e.g. Guttenberg and Goldenfeld, 2009).

Before proceeding, note that since $E_\omega(k) = k^2 E(k)$, if the small scales were dominated by an energy flux cascade, we would obtain $E_\omega(k) = k^2 k^{-5/3}$, which would diverge for large wave-numbers, and hence enstrophy could not be con-served. We therefore conclude that enstrophy must be cascaded from large to small scales through a k^{-3} regime, and energy flux from *smaller to larger* scales via a $k^{-5/3}$ regime, an "indirect" cascade. At the lowest wavenumbers, we must either introduce an energy sink, or we obtain a spectral peak (at k_E) that moves to lower and lower wavenumbers in time (the value is determined by dimensional arguments). Fig. 2.8 shows a schematic diagram for the latter case, assum-ing that injection of both enstrophy and energy fluxes occurs at the same (intermediate) scale. Finally, the dissipation wavenumbers may be estimated by dimensional arguments as in 3D turbulence: we find $k_{diss} = (\eta/v^3)^{1/6}$.

2.6 Atmospheric extensions
2.6.1 Applying isotropic turbulence to the atmosphere: the Gage–Lilly model

Because of the additional conserved enstrophy flux in 2D, the cascades are more complicated than in 3D, depending notably on the (possibly different) injection scales for ε, η. If we follow the classical model which first assumes isotropy, then – due to

the $\approx$ 10 km atmospheric scale height – we are forced to introduce at least two isotropic turbulent regimes: a 3D isotropic regime at scales smaller than 10 km, and another 2D isotropic turbulent regime at large scales. From the discussion above, we can see that numerous forcing and dissipation length scales and mechanisms will be required. Indeed, by the early 1980s, theorists had produced a series of complicated ad hoc conceptual models which involved a small-scale 3D direct energy cascade, a larger-scale direct enstrophy cascade and finally a very large-scale indirect energy cascade, the whole system involving three distinct sources of turbulent flux (e.g. Lilly, 1983).

The first major experiment devoted to testing the 2D/3D model was the EOLE experiment. It used the dispersion of constant-density balloons (Morel and Larchevêque, 1974; this is similar in principle to some of Richardson's methods used to obtain Fig. 1.1), and the balloons stayed (nearly) on isopycnals (i.e. surfaces of constant density), not on isobars. Due to the hydrostatic relation $\rho = -g^{-1}\partial p/\partial z$, the vertical spectrum of ρ: $E(k_z) \approx k_z^{-\beta\rho}$ has exponent $\beta_\rho = \beta_p - 2$ so that a key difference between isopycnals and isobars is that while the latter are gradually sloping ($\beta_P > 3$) the former are highly variable with large-scale average slopes diminishing at larger and larger scales.

The original conclusions of the EOLE analysis (Morel and Larchevêque, 1974) were that the turbulence in the 100–1000 km range was two-dimensional. However, even then discrepancies were noted between the relative diffusivity and the velocity structure function results. Later, and more importantly, the conclusions contradicted those of the GASP and MOZAIC analyses (which found $k^{-5/3}$ out to hundreds of kilometres; see below). This motivated the reanalysis of the original (and still unique) dataset by Lacorta *et al.* (2004), who used velocity structure functions (which they called "finite scale relative velocities") and other techniques to show that, on the contrary, the data followed the $\Delta x^{1/3}$ law (i.e. $\beta = 5/3$), thus vindicating Richardson over this range and invalidating the original conclusions. Fig. 2.9 shows their reanalysis, which supports Richardson over the range of about 200–2000 km.

Interestingly, it seems that to properly understand the behaviour below about 200 km we must revisit their reanalysis! This is because although Lacorta *et al.* (2004) interpolated the EOLE satellite
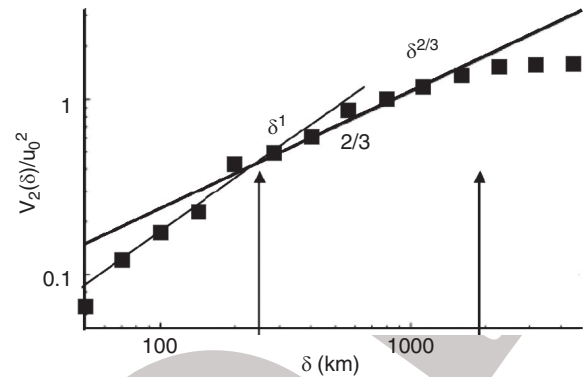

Fig. 2.9 Second-order velocity structure function estimated from the EOLE balloons. The theoretical effect of the low temporal resolution is discussed in Appendix 6A; it predicts the break as indicated on the left by the reference line, slope 1 (added to the original with break point corresponding to $\Delta t = 2.4$ hours and $u_0 = 100$ km/h, both numbers from their paper). The right-hand arrow shows the true limit $\sim$2000 km. Adapted from Lacorta *et al.* (2004).

tracked-balloon positions every hour, the actual data were at lower temporal resolution – "mostly" every 2.4 hours – and neither the original nor the recent reanalysis attempted to understand the consequences of this temporal smoothing. The basic effect is straightforward to calculate (the detailed calculations are postponed to Appendix 6A since we haven't yet developed all the necessary theory). If the mean advection velocity is u_0 (estimated by Lacorta *et al.*, 2004, as ≈ 100 km/h), and the balloon position is sampled at intervals of Δt, then the estimated velocities are effectively averaged over distances $u_0\Delta t$. This temporal and spatial averaging decreases the variability for distances $<u_0\Delta t$, i.e. on distance scales less than the typical advection distance. Surprisingly neither Lacorta *et al.* (2004) nor Morel and Larchevêque (1974) seem to have noticed this, instead attempting to find physical interpretations for the behaviour down to 50 km even though $u_0\Delta t$ according to their own data was at least 200 km. For example, Lacorta *et al.* (2004) claim that "at distances smaller than 100 km our results suggest an exponential decay with e folding time of about 1 day in rough agreement with Morel and Larchevêque (1974)." In Fig. 2.9, we show that even the slope for the range affected by the averaging is roughly as expected theoretically (assuming space-time scaling up to planetary scales: see Appendix 6A). In other words, the re-reanalysis of EOLE is compatible with Richardson's scaling results over the *entire* observed range, not only 200–2000 km.
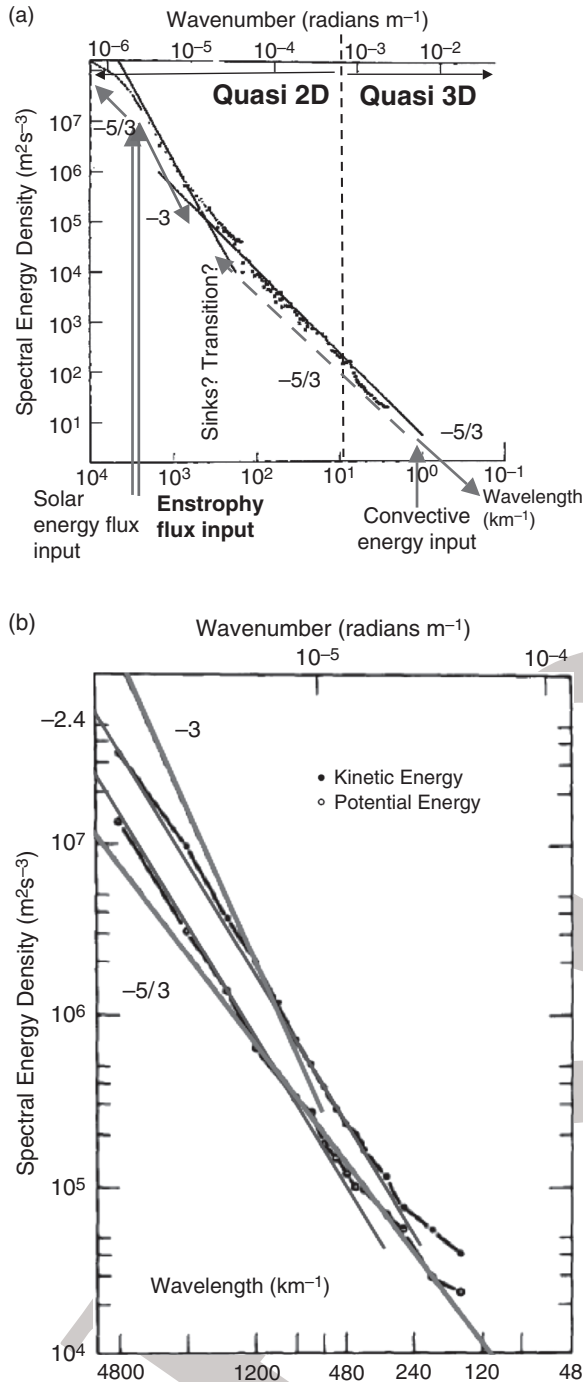
(a)

(b)

Fig. 2.10 (a) A schematic of the standard model updated to take into account the results of the GASP experiment. The figure is adapted from Lilly (1989) and schematically illustrates the "Gage–Lilly" model. Note that the 2D enstrophy cascade region spans much less than an order of magnitude in scale whereas the speculative inverse energy flux cascade (dashed line) spans over two orders of magnitude. (b) GASP spectrum of long-haul flights (> 4800 km) adapted from Gage and Nastrom (1986) with the reference lines corresponding to the horizontal and vertical behaviour discussed in the text (exponents 5/3, 2.4, i.e. ignoring intermittency corrections corresponding to $H_{h=}$ 1/3, $H_{v=}$ 0.7 as well as to the 2D isotropic turbulence slope –3).

Although at the time the EOLE experiment was influential, it did not include the determination of the spectrum, which was inconvenient to estimate because of the uneven distribution of the balloons. The first serious estimates of the horizontal wind spectrum had to await the GASP experiment (Fig. 2.10a), which was apparently incompatible with the early EOLE interpretations. The key difficulty was that the GASP spectra showed that $k^{-5/3}$ wind spectra extended out to scales much larger than the scale height of 10 km (up to several hundred kilometres). This motivated the development of the more sophisticated "Gage–Lilly" model (Fig. 2.10a: Lilly, 1989). This model suffers from many unsatisfactory ad hoc features, especially the upscale $k^{-5/3}$ energy flux regime from roughly 1 km to ∼200 km (dashed line in Fig. 2.10a), which Lilly describes as "escaped" 3D energy transformed to quasi-2D stratified turbulence. The same feature was termed "squeezed 3D isotropic turbulence" by Högström *et al.* (1999). Other difficulties are the unknown flux sinks in the 2D/3D transition region, an unknown large-scale energy flux dissipation mechanism (surface drag?), and speculative energy and enstrophy flux sources at ≈ 2000 km.

2.6.2   The real transition is from $k^{-5/3}$ to $k^{-2.4}$ . . . and it is spurious: a review of the classical aircraft campaigns and a new one (TAMDAR)

Even if we accept the plausibility of the various mechanisms invoked in the Gage–Lilly model, the evidence for 2D turbulence is scant: barely an octave in scale of the k^{-3} regime even in the classical (oft-reproduced) GASP spectrum (Fig. 2.10a). Actually, more careful examination of the original GASP analyses proves even more damaging to the k^{-3} hypothesis: while Fig. 2.10a was a composite of all the available data, the more relevant spectrum is the rarely cited Fig. 2.10b,

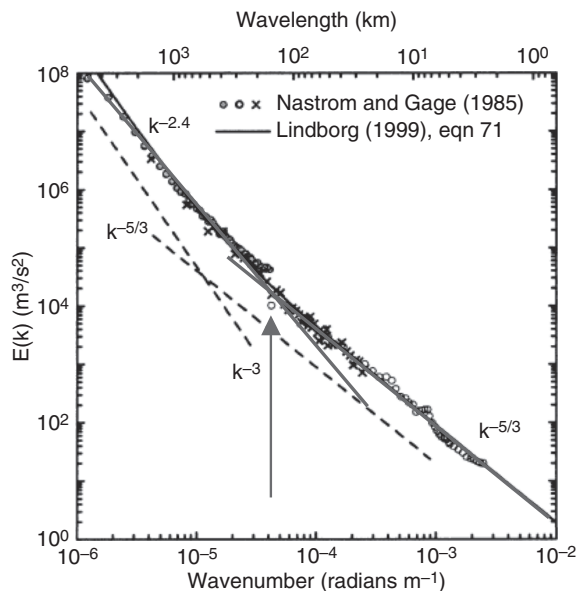**Classical turbulence, modern evidence**

Wavelength (km)

Fig. 2.11 A comparison of the GASP and MOZAIC spectra from commercial aircraft flying on isobars, adapted from Skamarock (2004), reproduced from Lovejoy et al. (2010). The thick lines show the behaviour predicted if the atmosphere has a perfect $k^{-5/3}$ horizontal spectrum but estimated from an aircraft following roughly horizontal trajectories until about 100 km (indicated by the arrows) and then following gradually sloping trajectories (either on isobars or gradual changes in altitude due to fuel consumption).
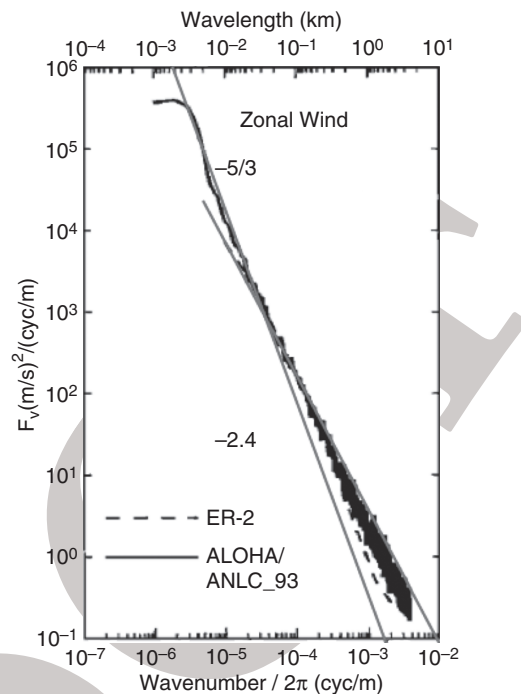

Wavelength (km)

Fig. 2.12 The averaged spectra adapted from Gao and Meriwether (1998) at 6 km altitude with the horizontal and vertical exponents discussed here indicated as reference lines. Reproduced from Lovejoy et al. (2010).

which shows only the relevant long-haul flights (> 4800 km). The interpretation of this spectrum is more straightforward than the composite since the composite effectively involves somewhat different ensembles of flights as one moves to larger and larger scales. However, the long-haul spectrum shows no hint whatsoever of a k^{-3} regime; instead, one sees $k^{-5/3}$ at small scales followed by an almost perfect $k^{-2.4}$ spectrum at the larger scales.

A more recent large-scale campaign to estimate spectra has also used instrumented commercial aircraft: the MOZAIC campaign of > 7600 flights between 9.4 and 11.8 km (Cho and Lindborg, 2001; Lindborg and Cho, 2001). Not surprisingly, it is very close to the GASP spectrum, and Fig. 2.11 conveniently summarizes and compares the two. Again it can be seen that any k^{-3} regime must be very narrow, and that in any case $k^{-5/3}$ behaviour at small scales followed by $k^{-2.4}$ at large scales (without any k^{-3} regime) explains the observations quite accurately. By reproducing key figures and adding appropriate

reference lines, we can see that the same $k^{-5/3}$ to $k^{-2.4}$ behaviour with similar transition scales (40–200 km) explains other aircraft wind spectra (Gao and Meriwether, 1998: 11 legs of the scientific Electra aircraft, which also flew along isobars but at ≈ 6 km; see Fig. 2.12); for stratospheric spectra, see Fig. 2.13 (Bacmeister et al., 1996). Lovejoy et al. (2009) also find similar behaviour in the tropospheric Gulfstream 4 scientific aircraft spectra already discussed in Chapter 1 (Fig. 2.14).

So why is there a break in the spectrum at scales from 40 to 400 km: highly variable yet significantly larger than the atmospheric scale height? And why is it not visible in other spectra of strongly nonlinearly linked fields, such as the radiances (Fig. 1.2) or the temperature or humidity (including from the same aircraft: compare Figs. 1.6c and 2.14)? The answer is surprisingly simple: it suffices that the aircraft have a small but nonzero slope, so that after a critical distance the fluctuations it measures no longer reflect the horizontal statistics, but rather the vertical ones.
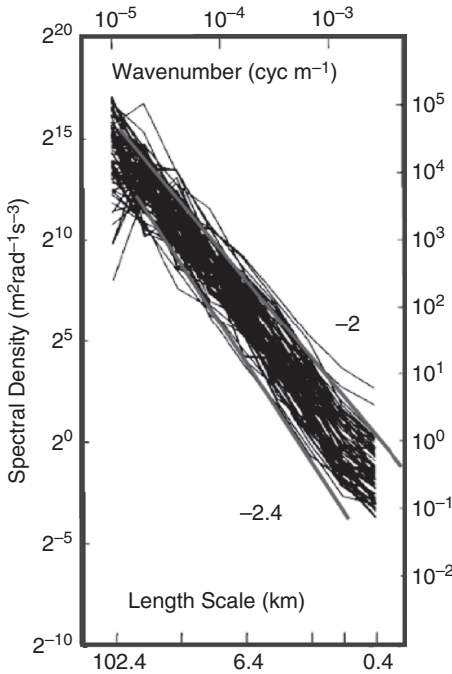
Comp. by: ESuguna Stage: Revises1 Chapter No.: 2 Title Name: LOVEJOYandSCHERTZER
Date:16/11/12 Time:15:20:50 Page Number: 41

2.6 Atmospheric extensions

Fig. 2.13 Stratospheric ER2 spectra adapted from Bacmeister et al. (1996, Fig. 5). This is a random subset of 1024 s legs, again with reference slopes added. Reproduced from Lovejoy et al. (2010).

Fig. 2.14 Recent spectra from the Pacific Winter Storm 2004 experiment: 24 aircraft legs, each 1120 km in length (resolution 280 m); units of k: $(km)^{-1}$. For more details on the Winter Storm 2004 data, see Section 6.3. The curves are for the longitudinal and transverse components of the wind (relative to the aircraft direction). The black reference lines show the theoretical Kolmogorov spectrum ($k^{-5/3}$; obeyed roughly up to ≈ 40 km) and the $k^{-2.4}$ spectrum at larger scales. Adapted from Lovejoy et al. (2009).

To see how this works, consider Fig. 2.15a, which is a contour plot of the mean squared horizontal wind differences $\langle \Delta v^2(\Delta x, \Delta z) \rangle$ for various lags $(\Delta x, \Delta z)$ in the vertical plane. It was obtained from data over the year 2009 from a fleet of short-range commercial aircraft flying over the continental USA; the overall sample contained over 14 500 aircraft legs (TAMDAR: Moninger et al., 2003; Mamrosh et al., 2006) sampled somewhat irregularly, but at roughly 20 km resolution in the horizontal. Our investigation required distinguishing statistics on isobars from those on isoheights, and thus required high-accuracy GPS altitude measurements. For our purposes, an essential TAMDAR improvement with respect to the more widespread, older AMDAR equipment was thus that the former included accurate GPS altimetry that enabled altitude differences (Δz) to be estimated to within ± 4 m, a level of accuracy essential for distinguishing isobars and isoheights. At the same time wind differences are measured to within ± 2.5 m/s. Although it is possible to estimate Δz, Δv from two different aircraft, here only data from single legs were considered. This eliminates the (relatively poor)
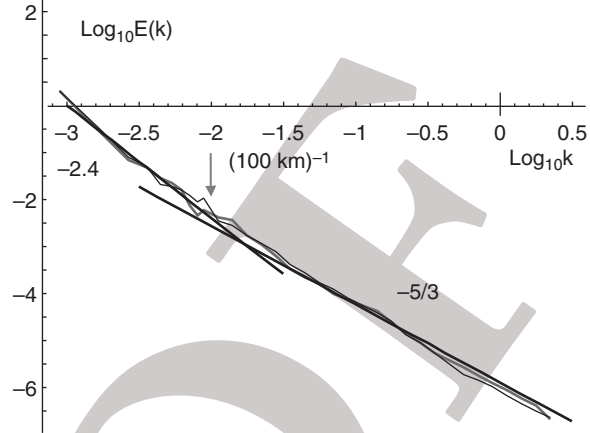
absolute sensor calibration from the problem, as the wind differences measured from single aircraft only require accurate *relative* calibrations. Using data from single aircraft not only yields much higher-accuracy measurements, but it also greatly simplifies the analysis of the – otherwise extremely complex to analyse – problem of highly nonuniform statistical sampling of Δv^2 in $(\Delta x, \Delta y, \Delta z, \Delta p, \Delta t)$ space that results when considering wind differences from two different aircraft with numerous particularities including geographical distributions determined by the commercial flight corridors. More details can be found in Pinel et al. (2012).

In Fig. 2.15a one can see that the empirical contours (dark) are nearly of the form theoretically predicted (light) for scaling stratified turbulence discussed in Chapter 6:

$$\langle \Delta v^2(\Delta x, \Delta z) \rangle = C \left(\left| \frac{\Delta x}{l_s} \right| + \left| \frac{\Delta z}{l_s} \right|^{1/H_z} \right)^{\xi(2)} \quad (2.85)$$

where H_z is the ratio of the horizontal to vertical wind exponent and $\xi(2)$ is the exponent of S_2 (Eqns. (2.71), (2.73)), the second-order "structure function exponent," and l_s is the "sphero-scale," which is the scale at which fluctuations have roughly the same vertical and horizontal extents. At scale l_s, we have $\langle \Delta v^2(l_s, 0) \rangle = C = \langle \Delta v^2(0, l_s) \rangle$ so that the
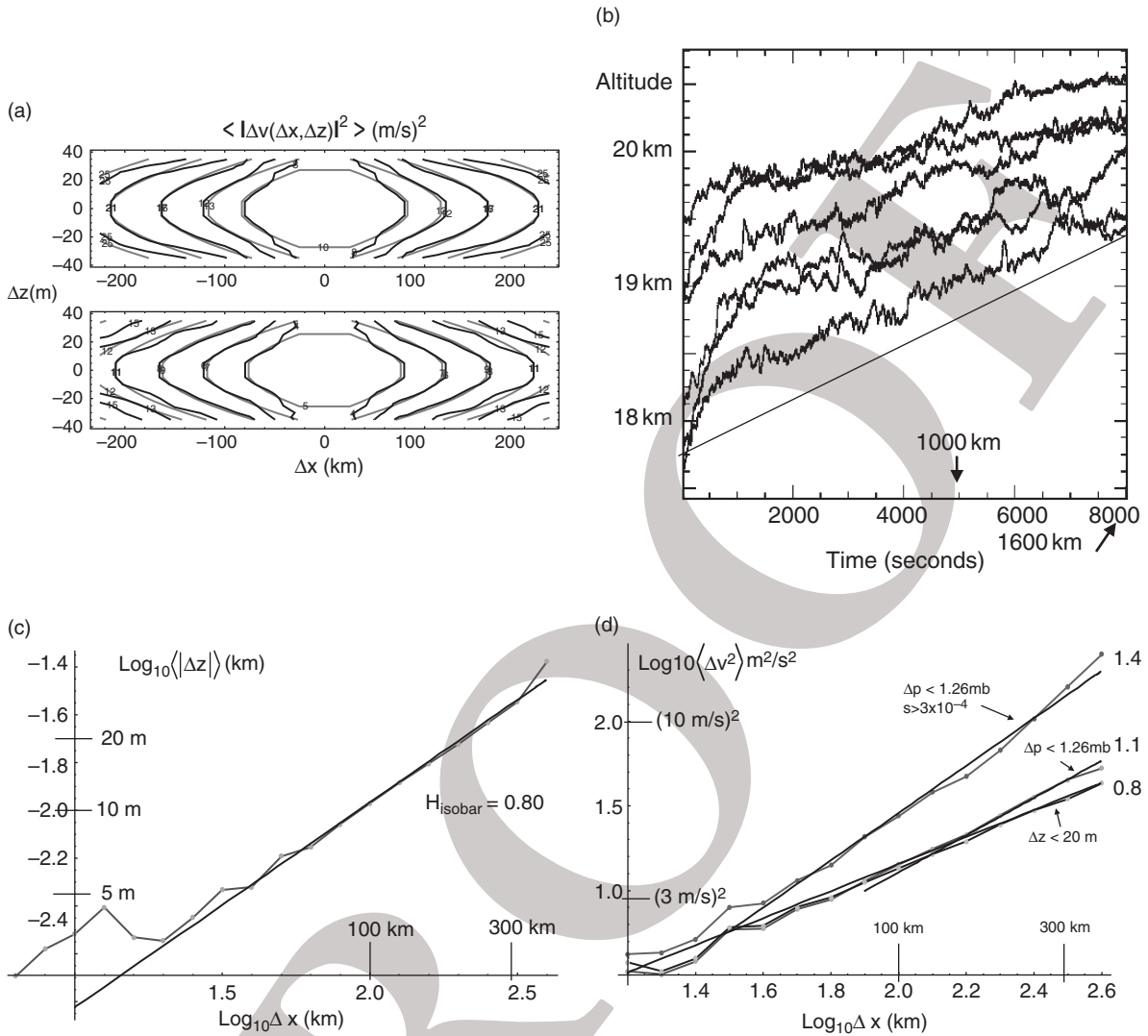
Classical turbulence, modern evidence

Fig. 2.15 (a) A contour plot of the mean squared transverse (top) and longitudinal (bottom) components of the wind, as estimated by a year's (≈ 14 500) TAMDAR flights, 484 000 wind difference measurements. All the fluctuations were from a single aircraft at different parts of its trajectory, and only trajectories between 5 and 5.5 km were used. Black shows the empirical contours, grey the theoretical contours assuming scaling stratification and the functional form indicated in the text. The numbers next to the contours are the values of the contours (italics is theory, bold is empirical, to improve the statistics, reflection symmetries were used). Reproduced from Pinel *et al.* (2012). (b) A sample of six fractal aircraft trajectories (fractal dimension ≈ 1.56) from NASA's ER2 aircraft during missions near Antarctica. The aircraft flew along isomachs but there was a mean vertical "drift" of ∼1 m/km (reference line) caused by the lightening of the aircraft due to fuel consumption. Adapted from Lovejoy *et al.* (2004). (c) For the TAMDAR data this shows the mean vertical displacement for points on isobars defined by $\Delta p < 0.126$ mb (373 000 differences were used, flight legs between 5 and 5.5 km). The reference line shows a slope $H_{isobar} = 0.80$ corresponding to a fractal dimension of $D_{isobar} = 1 + 0.80 = 1.80$. Each point is the average of over 1000 measurements. Reproduced from Pinel *et al.* (2012). (d) Comparison of mean squared wind differences of the transverse component of the wind from TAMDAR data sampled from near isobars ($\Delta p < 1.26$ mb), near isoheights ($\Delta z < 20$ m) and from sloping isobars i.e. $\Delta p < 1.26$ mb and slope $s > 3.2 \times 10^{-4}$ (the longitudinal components gave very similar behaviour). We see that the latter has the theoretical vertical exponent for a nonfractal vertical section, 1.4, the $\Delta p < 1.26$ mb curve has (for scales $> \sim140$ km) the exponent 1.1 theoretically predicted for the fractal isobars: $1.1 = H_{isobar} 1.4$, whereas the curve for $\Delta z < 20$ m has the theoretical isoheight exponent. Reproduced from Pinel *et al.* (2012).

corresponding structures are "roundish," hence the name. From the regression on $\langle \Delta v^2 \rangle$ in Fig. 2.15a, the best-fit empirical parameters are $H_z \approx 0.57$, $\xi(2) \approx 0.80$ and $l_s \approx 1.0 x\, 10^{-3}$ m. The H_z value is very close to the theory value ($H_z = (1/3)/(3/5) = 5/9 = 0.56$); see Chapter 6, although $\xi(2)$ is a little larger than the theory value $2H = 2/3$, and l_s is close to values measured in vertical lidar scans of pollution backscatter and to the somewhat less direct aircraft estimates in Lovejoy et al., 2004, 2009). The constant $C \approx 4.5 \times 10^{-6}$ m^2/s^2 is $\langle \Delta v(l s^2) \rangle \approx \langle \varepsilon^{2/3} l_s^{2/3} \rangle$; the equality is approximate since there are intermittency corrections due to the highly variable nature of ε, l_s (Lovejoy et al., 2008); ignoring these issues, taking $C \approx \varepsilon^{2/3} l_s^{2/3}$ we obtain $\varepsilon \approx 10^{-5}$ m^2/s^3. This low estimate of ε (see Chapter 8) and slightly larger value of $\xi(2)$ could thus be explained by intermittency corrections.

From the functional form in Eqn. (2.85) we can consider two particularly simple extreme cases: pure horizontal and pure vertical displacements. In the former case we easily see that the mean squared horizontal differences vary as $\langle \Delta v^2(\Delta x) \rangle \propto \Delta x^{\xi_h(2)}$ with $\xi_h(2) = \xi(2) \approx 0.8$, whereas in the latter case the mean squared vertical differences $\langle \Delta v^2(\Delta z) \rangle \propto \Delta z^{\xi_v(2)}$ with $\xi_v(2) = \xi(2)/H_z \approx 1.4$. Since the spectral exponent $\beta = 1 + \xi(2)$ (Eqn. (2.73)) this implies different horizontal and vertical spectral exponents: $\beta_h = 1.8$, $\beta_v = 2.4$.

In order to determine the spectrum measured from real aircraft trajectories, we need a model of the latter. For example, in Chapter 6 we consider a simple intermediate model involving a trajectory along a constant slope s; i.e. using $\Delta z = s\Delta x$ in Eqn. (2.85), we find a critical value Δx_c such that for $\Delta x < \Delta x_c$ the horizontal behaviour is dominant whereas for $\Delta x > \Delta x_c$ the vertical behaviour is dominant. It is therefore easy to imagine that, depending on how flat the aircraft trajectory is, at small scales $\beta \approx 1.8$, yet at large enough scales one could readily obtain a vertically dominated spectrum with a transition to $\beta \approx 2.4$, as found in the campaigns discussed above.

However, things are potentially more complicated than this simple constant-slope model. As discussed in Chapter 6, both the proportionality constant in Eqn. (2.85) and l_s depend on highly variable turbulent fluxes (energy and buoyancy force variable fluxes), and Fig. 2.15b shows that trajectories are not uniform with constant slope, but can be fractal. However the trajectories in the figure are from aircraft whose

autopilot flies on lines of constant Mach number, and this is quite unusual. It is more typical for aircraft to follow isobars; single long, high-resolution (280 m) isobaric aircraft trajectories are discussed in Chapter 6, but here we use the TAMDAR data, which are short ($< \sim 400$ km) and sampled somewhat irregularly (on flat legs, typically every ~ 20–30 km, much more frequently when changing altitude levels). This low sampling rate in individual legs is largely compensated for by the overall high number of TAMDAR legs: for example, 484 000 individual wind differences were used to estimate the contours in Fig. 2.15a. By sampling only wind differences from measurements nearly on the same isobar, we can determine the statistics of vertical isobaric cross-sections. Fig. 2.15c shows that on the isobar the mean vertical displacement $<\Delta z> \approx \Delta x^{H_{isobar}}$ with $H_{isobar} \approx 0.80$, so that the isobar is fractal (fractal dimension $1+H_{isobar} = 1.80$ in vertical sections; see Chapter 3).

We can now combine our information about $<\Delta v^2(\Delta x, \Delta z)>$ with our knowledge of the fractal structure of the isobars to see how $<\Delta v^2>$ varies on various trajectories (Fig. 2.15d). For example, we have already shown from Eqn. (2.85) that on isoheights $\langle \Delta v^2(\Delta x) \rangle \propto \Delta x^{\xi_h(2)}$ with $\xi_h(2) = \xi(2) = 0.8$, and this is confirmed in Fig. 2.15d. Let us now consider the behaviour along isobars. As in the constant-slope model discussed above, in Eqn. (2.85) for small horizontal displacements, the horizontal term dominates and we obtain the same result as for isoheights, i.e. $\langle \Delta v^2(\Delta x) \rangle \propto \Delta x^{\xi_h(2)} \approx \Delta x^{0.8}$. However, for large enough displacements the second term in Eqn. (2.85) becomes dominant so that we expect $\langle \Delta v^2(\Delta x) \rangle \propto \langle |\Delta z(\Delta x)| \rangle^{\xi_v(2)} \approx \Delta x^{H_{isobar}\xi_v(2)} \approx \Delta x^{H_{isobar}\xi(2)/H_z} \approx \Delta x^{1.1}$; this is also confirmed in Fig. 2.15d, although the behaviour is only dominant for scales $> \sim 140$ km. As a final test of the model, we can restrict our attention to those isobars which are also steeply sloping (in the figure, with slope > 0.32 m/km). In this case, the fractality of the isobars is no longer important, for a large range in Δx only the vertical displacement is dominant and we expect $\langle \Delta v^2(\Delta x) \rangle \propto \Delta x^{\xi_v(2)} \approx \Delta x^{1.4}$, which is also verified in the figure.

As a final comment we remark that in a recent paper Frehlich and Sharman (2010) used nearly the same TAMDAR data but reached an opposite conclusion: that $<\Delta v^2>$ was the same on isoheights as on

Classical turbulence, modern evidence

isobars. However, detailed analysis in Pinel *et al.* (2012) shows that this conclusion was likely spurious, the reason being the inappropriate use of TAMDAR data over the numerous flight segments where the aircraft changed altitude levels. The corresponding altitude resolution was much lower over these sloping sections than over the roughly flat ones, so much so that the purported isoheight data analyses were not really from isoheights at all – so the data analyses including these low-vertical-resolution sections were unable to adequately distinguish isoheight and isobar data. The TAMDAR system is programmed to sample much more frequently when the aircraft changes altitude levels, so that if care is not taken this low resolution can seriously bias the estimates, making it impossible to distinguish isoheight and isobar statistics. This was graphically demonstrated by Pinel *et al.* (2012), who could almost exactly reproduce the findings of Frehlich and Sharman (2010) by including these low-resolution segments, yet (as Fig. 2.15d shows) when they are removed the

difference between isoheight and isobar statistics becomes clear. Additional evidence pointing to bias was the fact that when the low-resolution data points were removed the horizontal scaling of $<\Delta v^2>$ was greatly improved.

This anisotropic scaling model of the vertical structure is developed further in Chapter 6, but it can easily quantitatively reproduce the observations leading to the reinterpretation of the Nastrom–Gage spectrum (Fig. 2.16a). In the new model, rather than having sources and sinks at precisely defined scales separated by wide ranges with no sources or sinks (the classical inertial ranges), the energy flux is instead from solar heating modulated by scaling cloud fields, so that the input is over a wide range of scales in a scaling manner (in accord with the observed scaling of the radiance: Figs. 1.2 and 1.3). In this reinterpretation, the large-scale (low-wave-number) $k^{-2.4}$ is simply a spurious consequence of the not carefully accounted for effects of anisotropic turbulence on the aircraft motion.
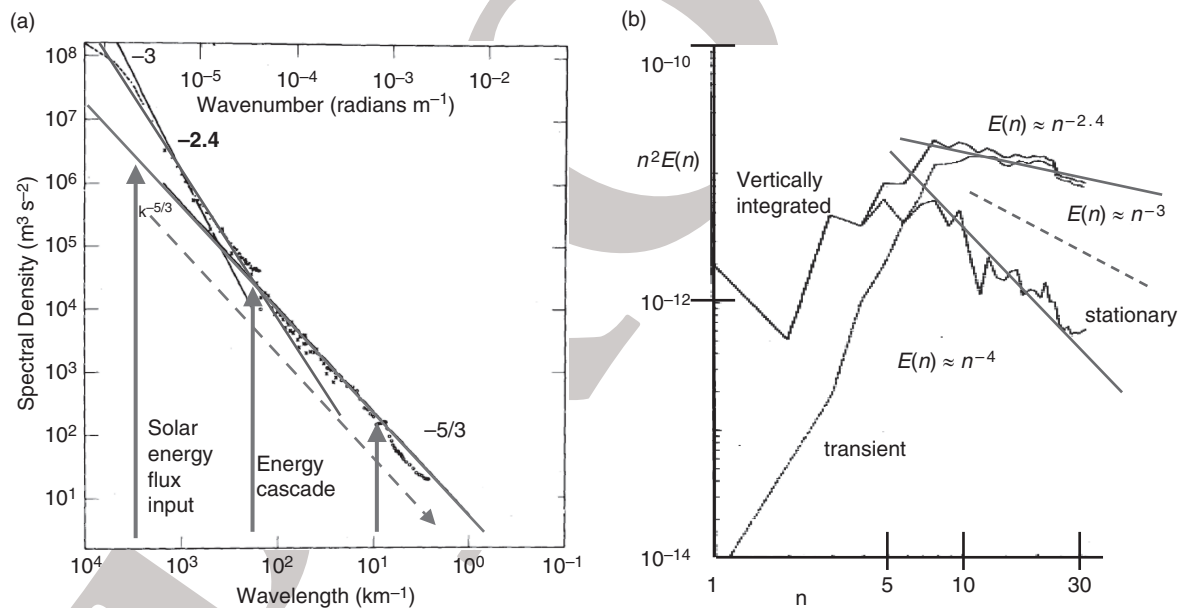

Fig. 2.16 (a) Reinterpretation of the Nastrom–Gage spectrum, as discussed in the text. The transition to large-scale $k^{-2.4}$ behaviour is a spurious consequence of aircraft travelling along gently sloping trajectories, as discussed in detail in Chapter 6. Reproduced from Lovejoy and Schertzer (2010). (b) The enstrophy spectrum ($= n^2 E(n)$, where $E(n)$ is the wind spectrum and n is the principal spherical harmonic wavenumber), adapted from Boer and Shepherd (1983). The three curves are from January data; the solid line is for the vertically integrated atmosphere, the lines indicate stationary (spatial spectrum of the monthly average), and the transient is the deviation from the monthly average. Over the range $n \approx 5$–30 (700–4000 km) the exponents of the spectra of the transient and vertically averaged atmosphere are extremely close to the vertical value $\beta \approx 2.4$, but the stationary spectrum exponent is $\beta \approx 4$. No $\beta \approx 3$ regime is observed (dashed line). Reproduced from Lovejoy *et al.* (2010).

2.6.3   The classical approach: conclusions from analyses and reanalyses

The interpretation of aircraft data in terms of large-scale 2D turbulence was very influential, and other evidence about atmospheric structure and statistics were generally interpreted in the same way. The problem was that the special 2D exponent $\beta = 3$ provided the only theoretical framework for explaining spectra with $\beta > 5/3$. The long absence of a credible alternative theory tempted even early investigators to "shoehorn" their spectra into the k^{-3} mould. For example, by "eyeballing" four spectra over less than an *octave* in scale, Julian *et al.* (1970) concluded that $2.7 < \beta < 3.1$ for the horizontal wind. In the 1980s larger datasets became available, and it was possible to make more direct tests of 2D turbulence theory from atmospheric analyses (Boer and Shepherd, 1983) and later from the ECMWF ERA40 reanalyses (Strauss and Ditlevsen, 1999). Although Boer and Shepherd (1983) gave cautious support to $\beta \approx 3$ and to a 2D interpretation, in hindsight and with the benefit of a simple theory predicting $\beta \approx 2.4$, their conclusions seem unconvincing (Fig. 2.16b). Similarly, when interpreting their reanalyses, Strauss and Ditlevsen (1999) found that "$\beta \approx 2.5$–2.6 . . . significantly different than the classical turbulence theory prediction of 3," but again close to the value 2.4.

Today, we can revisit wind spectra using the state-of-the-art successor to the ERA40 reanalysis – the ECMWF interim reanalysis whose spectra were already presented in Fig. 1.5b, and to which we return in Chapter 4 – and calculate the spectrum directly without Strauss and Ditlevsen's complex 2D preprocessing. Fig. 2.17 shows the angle integrated spectrum of the zonal wind at each tropospheric 100 mb level, compensated by the average $k^{-2.4}$ behaviour so as to accentuate the small deviations. Also shown in the figure are straight *reference* lines. These are *not* regressions but rather the predictions of the stratified anisotropic scaling model discussed in Chapter 6: the slopes are those empirically estimated in the *vertical* direction from dropsondes (Fig. 6.2; Lovejoy *et al.*, 2007). Regressions on the reanalysis spectra from $k = 2$ to $k = 30$ (i.e. 5000–330 km) give β differing by less than 0.05 throughout the data-rich lower 4 km, rising to only 0.2 at 10 km (≈ 200 mb). Following the discussion of the previous section, we should not be surprised if
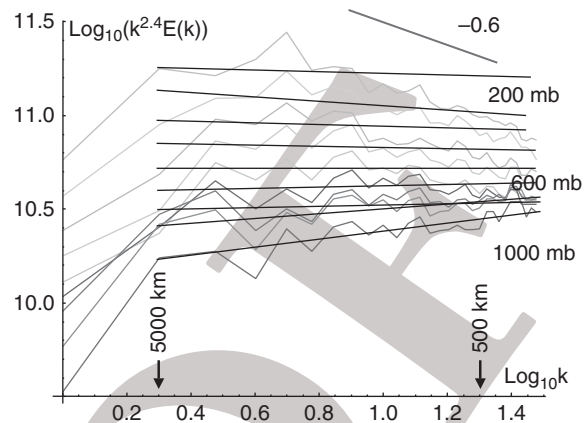

Fig. 2.17 The isotropic spectrum of the zonal component of the wind at 200, 300, 400, . . ., 1000 mb from the ECMWF interim reanalysis for January 2006 between $\pm$ 45° latitude. The straight lines are *not* regressions, rather they have the slopes of the horizontal wind in the vertical direction as estimated by dropsondes in Lovejoy *et al.* (2007). It can be seen that the isobaric velocity spectra have exponents close to the vertical values, and this is especially true of the data-rich lower levels. The 200 mb spectrum falls off a little too quickly at high wavenumbers, possibly due to poor-resolution data below $\sim$1000 km. The scaling starts at $k = 2$–3, corresponding to $n = 4$–6 in Fig. 2.16b. Reproduced from Lovejoy *et al.* (2010).

these small differences are the consequences of either intermittent aircraft and/or sonde motion (Chapter 6).

2.6.4   Evidence from satellite altimeter winds over the ocean

One way of overcoming the problems and limitations of in-situ wind measurements is to use remote sensing. The most direct remote method is to use the Doppler shift from clear-air radar turbulence measurements. However, existing datasets are over fairly narrow ranges of scales. In addition, the radar measures the radial wind component, which systematically changes direction as the radar scans to build up a three-dimensional field. This makes the interpretations complicated and tempts users to make "products" based on complex-to-analyse assumptions about the statistics in order to correct for these effects.

An alternative is to use ocean surface data from satellite scatterometers to measure wave heights and to correlate these with surface winds over the oceans. Such satellite wind products have been developed since the mid 1980s and rely on measurements of Bragg

Classical turbulence, modern evidence
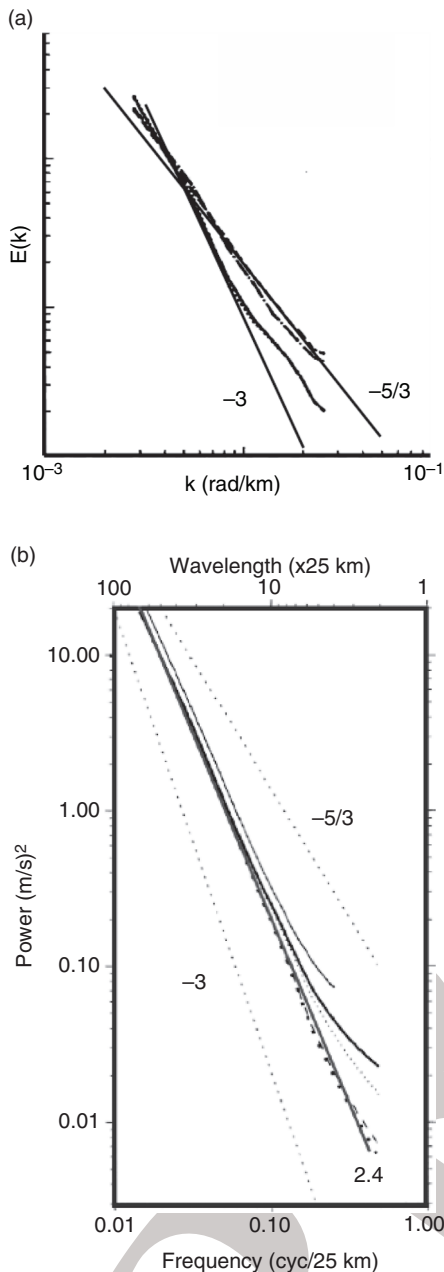
(a)

(b)

Fig. 2.18 (a) The spectra of sea surface winds as estimated from the SeaSat scatterometer over four regions in the Pacific Ocean (regions 1, 2 are the South Pacific, regions 3, 4 are the north Pacific), adapted from Freilich and Chelton (1986). The smallest wavenumber corresponds to about 2200 km, the reference lines (added) have slopes −3, −5/3. (b) The kinetic energy spectrum estimated over the oceans over a year, using QuikScat satellite altimeter data (adapted from Patoux and Brown, 2001). DIRTH is the recommended product; also shown are reference lines −5/3, −3 (in the original), with −2.4 reference line added. Largest scale is 1700 km, smallest is $2 \times 25 = 50$ km.

scattering amplitudes of ocean waves at the typically centimetric scatterometer wavelength (e.g. 2.1 cm from the SeaSat scatterometer, Fig. 2.18a, and 2.2 cm for the QuikScat data in Fig. 2.18b). At these wavelengths, the scatterometer is sensitive to capillary waves whose amplitudes are only indirectly related to the local winds. Correlating the scatterometer backscatter with the wind speed is only part of the problem; more difficult is determining the wind direction. At the moment, this is currently done by observing the same patch of ocean at different angles and by using meteorological reanalyses to help remove remaining directional ambiguities. The final product is thus dependent in a number of subtle ways on various assumptions about the nature of the turbulence and of the numerical models. Bearing this in mind, we refer the reader to some early scatterometer results that had spectral exponents quite near $\beta = 5/3$ (see the regression lines in Fig. 2.18a; Freilich and Chelton, 1986): over the range 200–2200 km, the regression estimates for the tropics were $\beta \approx 1.9$, and for the mid-latitudes $\beta \approx 2.2$. More recent products use more sophisticated algorithms, but the results are not much different: Fig. 2.18b shows spectra using the DIRTH algorithm (Patoux and Brown, 2001). As can be seen, the spectrum is almost perfectly scaling with $\beta = 2.4$: the (sloping) isobaric value. Although the value of the exponent may well depend on some of the assumptions that went into its derivation, these assumptions would be unlikely to transform an otherwise nonscaling spectrum into a scaling one. In other words, the fact that the spectrum is nearly a perfect power law over the observed range is highly significant and in itself would be difficult to explain with the 2D/3D model. Similar but yet more recent results using 10 years of data (instead of one year; King and Kerr, 2010), are shown in Fig. 2.19, showing that the exponents are apparently even lower, very close to the Kolmogorov value (the isotropic 2D turbulence result $\xi(2) = 2$ corresponding to $\beta = 3$, is completely off the scale!). Also indicated is the Bolgiano–Obukhov value $\xi(2) = 2 \, (3/5) - K(2) \approx 1.15$ (the horizontal line) which would be expected for a near-surface layer sloping in the vertical direction ($K(2) \approx 0.05$ is the empirical intermittency correction; see Chapters 5, 6).

Finally we could add that a recent QuickScat paper (Xu *et al.*, 2011) claims that β varies geographically from 1.6 to 2.9, but these estimates are based on little

Comp. by: ESuguna   Stage: Revises1   Chapter No.: 2   Title Name: LOVEJOYandSCHERTZER
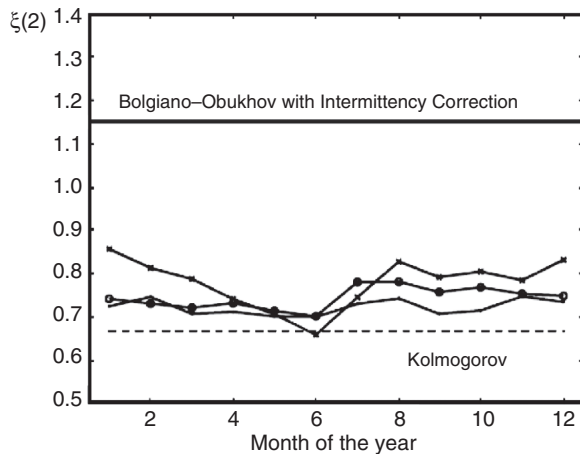Date:16/11/12   Time:15:20:55   Page Number: 47

2.6 Atmospheric extensions

Fig. 2.19 Regression exponents for the second-order wind structure function ξ(2) estimated by regression over the "meso beta scale" (20–200 km), from 10 years of QuikScat sensor data with 1800 km swaths at 25 km resolution, adapted from King and Kerr (2010). The three curves are for somewhat different parts of the Pacific Ocean.
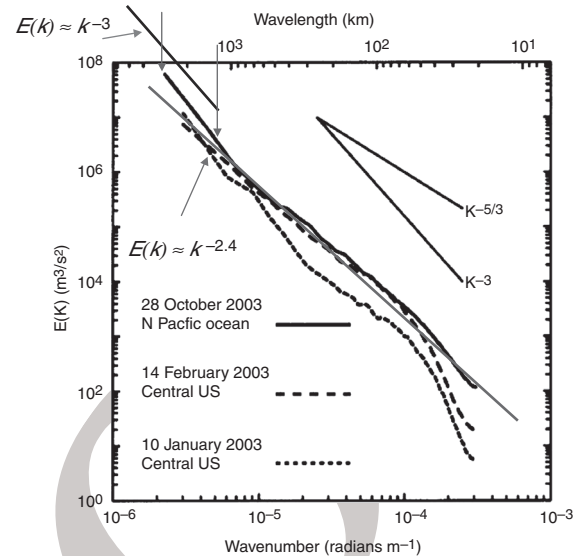

Fig. 2.20 Sample spectra from WRF forecasts of zonal wind averaged over the isobaric surfaces covering roughly the range 3–9 km in altitude, adapted from Skamarock (2004). Although they claimed that this shows a "clear k^{-3} regime" for the solid (oceanic) spectrum it only spans a range of factor 2–3 in scale, and this at the relatively unreliable extreme low wavenumbers (between the downpointing arrows, upper left). Except for the extremes, the spectra again follow the isobaric predictions $k^{-2.4}$ very well over most of the range. Reproduced from Lovejoy et al. (2010).

more than an octave in scale. In fact, all the data are very close to β = 1.8, with high wavenumber deviations from scaling accounting for most of the regional spectral differences.

2.6.5   The continuing difficulties with the classical model and inferences from numerical simulations

In order to improve on these speculative mechanisms needed to combine isotropic 2D and isotropic 3D turublence, efforts have been made to reproduce "realistic" k^{-3} to $k^{-5/3}$ transitions in numerical models. This is not a trivial question, because of the possibility of "three-dimensionalization" of two-dimensional flows discussed in Ngan et al. (2004), i.e. the likelihood that three-dimensional turbulence can destabilize an otherwise 2D flow. For the moment, the results are at best equivocal. For example, most numerical weather models do not display the transition (Palmer, 2001), while others may display it although over very small ranges – e.g. the Skamarock (2004) WRF (regional) model spectra, which are in fact very close to $k^{-2.4}$ (Fig. 2.20). To date, the most convincing k^{-3} to $k^{-5/3}$ transitions in numerical models have been produced using the SKYHI model on the earth simulator

(Takayashi et al., 2006; Hamilton et al., 2008), yet as pointed out by Lovejoy et al. (2010) they have the poorest fit to GASP observations precisely over the range ∼400–3000 km which their (painstakingly crafted) $k^{-5/3}$ to k^{-3} transition is supposed to explain. In other words, this model "success" may make them *less* rather than *more* realistic! In addition, Smith (2004) has shown that at least in the case of the quasi-geostrophic simulation by Tung and Orlando (2003), high wavenumber $k^{-5/3}$ regimes are in reality spurious consequences of energy build-up due to unresolved high wavenumbers with respect to an incorrectly "tuned" hyperviscosity.

2.6.6   Empirical determination of the direction of the cascade

Another way to test the classical 2D/3D model and to compare it to the anisotropic scaling model is to examine the spectral energy transfers due to the nonlinear terms. A 2D cascade will display an upscale

Classical turbulence, modern evidence
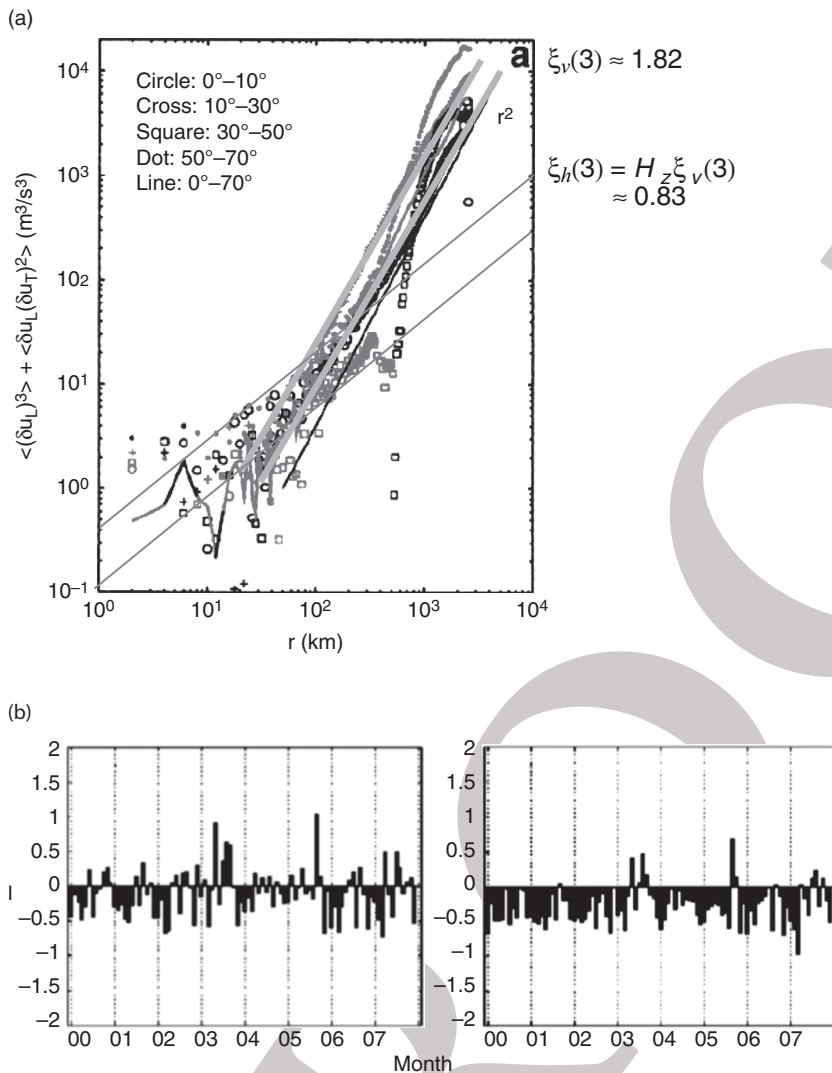
(a)

(b)

Fig. 2.21 (a) Third-order structure functions (diagonal contributions) adapted from Plate 1 of Cho and Lindborg (2001). Light grey indicates a negative sign, dark grey, positive, indicating large- to small-scale and small- to large-scale transfers, respectively. The theoretical reference lines were added with slopes corresponding to the predictions of the sloping isobaric trajectory model presented here (Section 2.6.2 and Chapter 6) with the third-order vertical structure function $\xi_v(q) = qH - K(q) = 1.82$ (using $q = 3$, $H = 0.77$, $K(3) \approx 0.49$) and horizontal structure function with $\xi_h(q) = \xi_v(q) H_z = 0.83$ ($H_z = 0.46$; parameters from Chapter 6 and Lovejoy et al., 2010). The transition is not far from the 40 km found in the Gulfstream 4 analyses (Chapter 6). (b) The third-order structure function of the horizontal wind normalized by the second-order function (the skewness) estimate QuickScat scatterometer data from the N4WP region of the Pacific. These are monthly averages of I = skewness; < 0 means large- to small-scale cascade. The left is averaged over the 250–1000 km ("meso-α") scale range, the right over the 25–250 km ("meso-β") range. Although the transfer is predominantly from large to small, it is highly intermittent in accord with the finding here from the ECMWF reanalysis (Figs. 2.22, 2.23) and with the predictions of the scaling model. Adapted from Fig. 6 of Kerr and King (2009).

energy transfer, a 3D cascade a downscale transfer (Section 2.5.2); furthermore, the usual schematics (e.g. the Gage–Lilly model, Section 2.6.1) also assume that the corresponding ranges are "inertial," i.e. with no sources or sinks, so that the fluxes are roughly constant in Fourier space. In comparison, in the anisotropic scaling model things can be much more complicated, since the sources and sinks (which will be largely solar heating and infrared cooling) will be scaling and nonlinearly coupled to the dynamical fields (via the scaling cloud field).

The empirical determination of the direction of the energy fluxes is very demanding, since in principle all wind components and their derivatives are required.

However, with the help of the assumption of statistical isotropy, Lindborg (1999) related the sign of the third-order velocity structure function $<\Delta v^3>$ to the direction of the cascade. The results (using MOZAIC aircraft data) showed mostly negative third-order structure functions (even out to 1000 km) in agreement with a downward (i.e. 3D) cascade. But the signs were not consistent (see Fig. 2.21a, which also shows that their third-order structure functions are close to those theoretically predicted for sloping isobaric aircraft trajectories). An algorithmic correction introduced by Cho and Lindborg (2001), although not clearly explained, surprisingly yielded a more opposite conclusion.

(a)

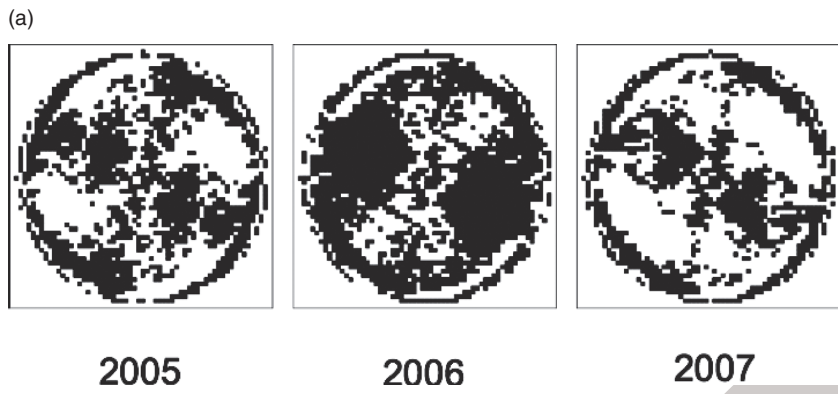2005   2006   2007

Fig. 2.22 (a) The sign of $T(\underline{k})$ for each of the three years analysed. Black indicates $T > 0$, white, $T < 0$. The horizontal axis is k_x (zonal), the vertical axis, k_y (meridional); the largest wavenumber corresponds to 330 km, the smallest to 10 000 km (more accurately, $\pm 45°$ about the equator and $0–90°$, $90–180°$, $180–270°$, $270–0°$ longitude). (b) The same as Fig. 2.22a, but for the ensemble 2005–2007 (right) and the disagreement areas (in grey, left).
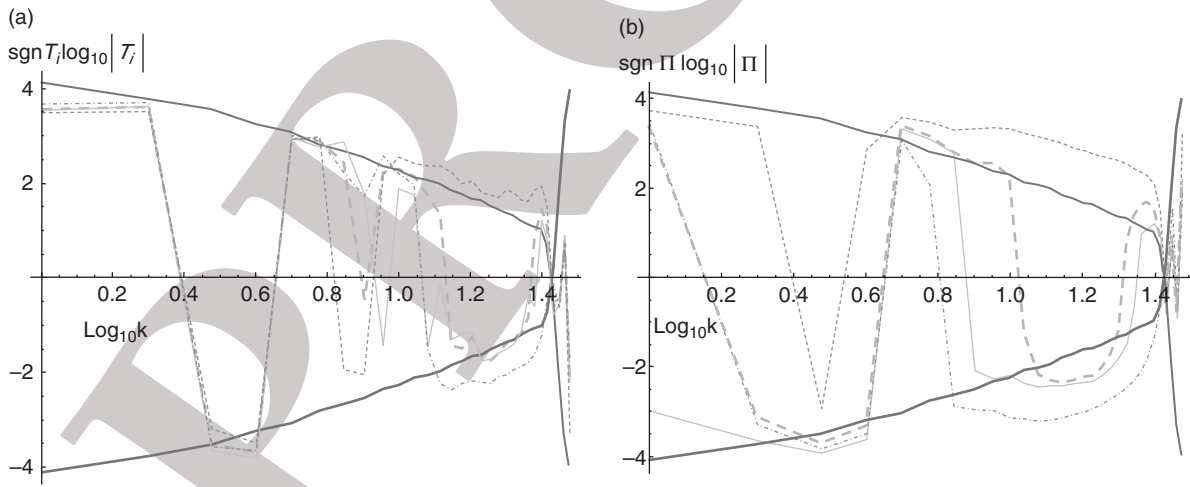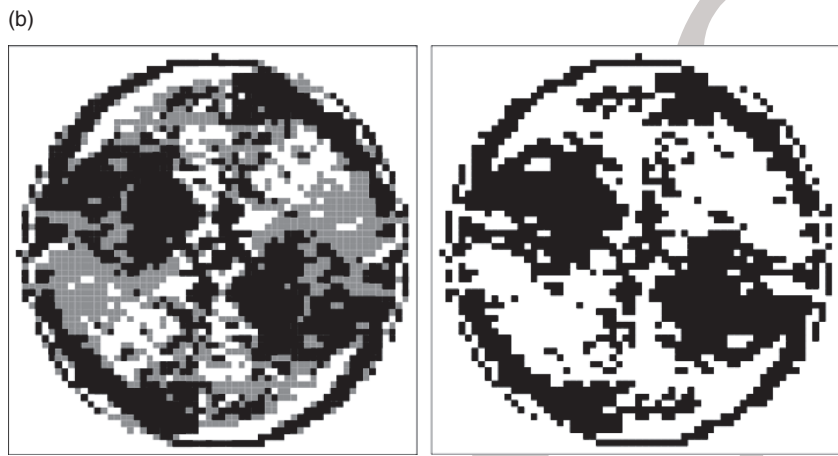
(b)

(a)

(b)

Fig. 2.23 (a)The angular integral of $T(k)$ for each year: 2005, 2006, 2007 The average of the three is the medium grey line which is only clearly distinguishable to the right of the 0.8 position (it's the line that barely drops below the axis at $\log_{10}k = 0.9$). The thick darker lines that roughly define the envelope are the isotropic energy spectrum $E(k)$ (top) and its negative (bottom). (b) The corresponding plots of $\Pi(k)$, which is the integral of $T(k)$, over wavenumbers higher than k for each year: 2005, 2006, 2007. The average of the three (medium grey) is again only clearly distinguishable when its drop below the upper envelope at about $\log_{10}k \approx 1.0$. The thick darker lines that define the envelope are the same as in Fig. 2.23a.

Classical turbulence, modern evidence

Recently, Kerr and King (2009), using QuickScat scatterometer data, similarly found that the sign of the flux fluctuates as the horizontal lag (scale) changes (Fig. 2.21b).

To test this out in a more direct way (without the third-order structure functions and isotropy assumptions), we can use the ECMWF interim reanalysis products; here the zonal and meridional winds at 700 mb for the years 2005–2007. The main weakness is the hybrid nature of the reanalyses and the neglect of the contribution of the vertical wind terms (the minimum reanalysis scale is 166 km, which is much larger than the atmospheric thickness). Let us recall that the classical (isotropic) spectral energy transfer $T(k, t)$ is defined by the triple velocity correlations coming from nonlinear interactions and which satisfy:

$$\left(\frac{\partial}{\partial t} + 2\nu k^2\right)E(k, t) = T(k, t) \tag{2.86}$$

where $E(k, t)$ is the spectrum as a function of time (see e.g. Lesieur, 1987). The same equation holds before averaging over all wave-vector directions (i.e. without hypothesizing isotropy). In this case consider respectively $\langle v^2 \rangle = u(0)$ and the spectral transfer $T(\underline{k}, t)$ that depends on the vector ($\underline{k}$ ($\hat{u}(\underline{k}, t)$ is the Fourier transform of u: Appendix 2A). The relationship between the two transfers is merely:

$$T(k) = \int\limits_{|\underline{k}'|=k} T(\underline{k}')d\underline{k}' \tag{2.87}$$

(i.e. angle integration). Because the isobaric surfaces are orthogonal to the pressure gradients, the spectral transfer for the "horizontal" velocity along the isobars is somewhat simpler than its more general expression on isoheights (advection is then the unique nonlinear term in the Navier–Stokes equations). One can show (Appendix 2C) that in this case, written out explicitly and considering only the horizontal transfer:

$$T(\underline{k}) = 2k_x \, Im\left[\langle \widetilde{u^*}(\widetilde{u^2}) \rangle + \langle \widetilde{v^*}(\widetilde{uv}) \rangle\right]$$
$$+ 2k_y \, Im\left[\langle \widetilde{u^*}(\widetilde{uv}) \rangle + \langle \widetilde{v^*}(\widetilde{v^2}) \rangle\right] \tag{2.88}$$

where we have used the notation $u = v_x$, $v = v_y$ (zonal and meridional components). The vertical wind was

ignored because in the reanalyses the vertical scales are so much smaller than the smallest horizontal scale (here 1.5°, i.e. 166 km).

Fig. 2.22a shows $sgn(T(\underline{k}))$ when sections of the reanalyses are used in the calculations. Each 700 mb field was broken into sections from $\pm$ 45° latitude (this avoids strong distortions from the map projection), and four disjoint 90° longitudinal sections. It can be seen by comparing the results for the different years that the distribution is not at all isotropic, and that much of the details of the anisotropy persist from one year to another (note that standard Hann windowing techniques were used for the numerical Fourier transforms). Fig. 2.22b shows that over half of the wavevectors agree on the sign for each of the three years, but that the region of agreement has a highly complex fractal-like structure. In order to investigate further, we calculated the classical transfer, T (Eqn. (2.87)).

Fig. 2.23a shows the result: the sign oscillates every octave or so in scale, in a largely reproducible way from year to year, yet there is no obvious 2D/3D transition, nor source/sink-free inertial range. At the largest octave or so in scales (smallest k), the transfer is positive (from large to small). Finally, we can calculate the total flux from scales larger than k^{-1} to smaller scales:

$$\Pi(k) = \int\limits_{k}^{\infty} T_i(k')dk' \tag{2.89}$$

This is shown in Fig. 2.23b. Although the integration naturally smoothes out some of the oscillations present in $T(k)$, there is still no obvious pattern, with the overall direction/sign changing every factor of 4–5 in scale. Note that here, as for T, at the very high wavenumbers the hyperviscous effects mean that the transfer is poorly estimated and should be ignored. In both Figs. 2.23a and 2.23b we have superposed the envelope defined by the isotropic energy spectrum (see the discussion of this and the slightly different spectrum calculated in Chapter 6 from the 2006 reanalyses). This comparison shows that the magnitude of the transfer closely follows the spectrum itself. Other attempts to test the direction of the cascade using aircraft estimates of the sign of the third-order velocity structure function (Fig. 2.21b)

have found similar chaotic/complex variations of cascade direction with scale, much more in accord with a scaling input and output of energy over a wide range.

2.7 Summary of emergent laws in Chapter 2

We derived several scaling laws in dimensional form in both real space and Fourier space (spectra) by using turbulent fluxes linked to the Navier–Stokes equations in three dimensions (the Kolmogorov–Obukhov law, Eqn. (2.90), top) and two dimensions (the Kraichnan law, middle), and linked to the equation of passive scalar advection (the Corrsin–Obukhov law, bottom):

$$\Delta v = \varepsilon^{1/3}|\underline{\Delta r}|^{1/3}; \quad E_v(k) = \varepsilon^{2/3}k^{-5/3}$$

$$\Delta v = \eta^{1/3}|\underline{\Delta r}|; \quad E_v(k) = \eta^{2/3}k^{-3}$$

$$\Delta \rho = \chi^{1/2}\varepsilon^{-1/6}|\underline{\Delta r}|^{1/3}; \quad E_\rho(k) = \chi\varepsilon^{-1/3}k^{-5/3}$$

$$(2.90)$$

Each equation depends on a turbulent flux: the energy flux (3D, ε), the enstrophy flux (2D, η) and the passive scalar variance flux (χ), respectively. For the moment, each is considered to be classical, i.e. the fluxes are $\approx$ constant (spatially homogeneous, quasi-Gaussian, nonintermittent). To emphasize that the above assumes isotropy, we have replaced the spatial lag Δx used in the earlier sections by the modulus of the vector lag $\underline{\Delta r}$.

The general form of these laws is:

$$\Delta f = \varphi|\underline{\Delta r}|^H \qquad (2.91)$$

for fluctuations Δf in a turbulent field f, flux φ and exponent H. This is the prototypical emergent atmospheric law. In this classical form it is valid only for weakly variable fluxes and for statistical isotropy, assumptions which the pioneers doubted would allow them to be valid in the atmosphere over scales much larger than several hundred metres. However, the rest of this book shows how to generalize φ to a highly variable multifractal cascade process and for the

isotropic vector norm scale notion $|\underline{\Delta r}|$ replaced by an anisotropic scale function $\|\underline{\Delta r}\|$. Finally, we assumed that the fluctuation was simply a difference, but this is not always adequate – so that, for example, when H is outside the range 0–1, the notion of fluctuation Δf itself can be refined with the help of wavelets (Section 5.5).

The general relations between real-space fluctuations and Fourier-space spectra are obtained using the Wiener–Khinchin theorem (see Appendix 2A for a demonstration), and the specific relations that apply in scaling systems are obtained using Tauberian theorems. The Wiener–Khinchin theorem is valid for statistically stationary processes and relates the autocorrelation $R(\tau)$ to the power spectrum $E(\omega)$:

$$R(\tau) = \left\langle v(t)v(t-\tau) \right\rangle = \int_{-\infty}^{\infty} d\omega\, e^{+i\omega\tau}E(\omega)$$

$$(2.92)$$

$R(\tau)$ is related to the "Δ-variance" of the fluctuation, i.e. the second-order structure function $S_2(\tau)$:

$$S_2(\tau) = \left\langle \Delta v(\tau)^2 \right\rangle = \left\langle \left(v(t) - v(t-\tau) \right)^2 \right\rangle$$
$$= 2\left[\left\langle v(t)^2 \right\rangle - \left\langle v(t)v(t-\tau) \right\rangle \right] \qquad (2.93)$$

or in terms of the power spectrum:

$$S_2(\tau) = 2\Big(R(0) - R(\tau)\Big) = 2\int_{-\infty}^{\infty} d\omega\, E(\omega)(1 - e^{+i\omega\tau})$$

$$(2.94)$$

In scaling regimes, we have power law spectra $E(\omega) \approx \omega^{-\beta}$, and we can use a Tauberian theorem to conclude that $R(\tau)$, $S_2(\tau)$ also follow power laws:

$$E(\omega) \approx \omega^{-\beta} \Leftrightarrow R(\tau) \approx \tau^{\xi(2)}; \quad \beta < 1 \qquad (2.95)$$

where the condition $\beta < 1$ is needed for low-frequency convergence. A high-frequency (small-scale) cutoff is also needed, but one is always present in discretely sampled data. For the structure function: